

Machine-learning potentials for structurally and chemically complex MAB phases: strain hardening and ripplocation-mediated plasticity

Nikola Koutná^{1,2,*}, Shuyao Lin^{1,2}, Lars Hultman^{2,3}, Davide G. Sangiovanni², and Paul H. Mayrhofer¹

¹Institute of Materials Science and Technology, TU Wien, Getreidemarkt 9, A-1060 Vienna, Austria

²Department of Physics, Chemistry, and Biology (IFM), Linköping University, SE-58183 Linköping, Sweden

³Center for Plasma and Thin Film Technologies, Ming Chi University of Technology, New Taipei City 24301, Taiwan

*nikola.koutna@tuwien.ac.at

ABSTRACT

Though offering unprecedented pathways to molecular dynamics (MD) simulations of technologically-relevant materials and conditions, machine-learning interatomic potentials (MLIPs) are typically trained for “simple” materials and properties with minor size effects. Our study of MAB phases (MABs)—alternating transition metal boride (MB) and group A element layers—exemplifies that MLIPs for complex materials can be fitted and used in a high-throughput fashion: for predicting structural and mechanical properties across a large chemical/phase/temperature space. Considering group 4–6 transition metal based MABs, with A = Al and the 222, 212, and 314 type phases, three MLIPs are trained and tested, including lattice and elastic constants calculations at temperatures $T \in \{0, 300, 1200\}$ K, extrapolation grade and energy (force, stress) error analysis for $\approx 3 \cdot 10^6$ *ab initio* MD snapshots. Subsequently, nanoscale tensile tests serve to quantify upper limits of strength and toughness attainable in single-crystal MABs at 300 K as well as their temperature evolution. In-plane tensile deformation is characterised by relatively high strength, $\{110\}\{001\}$ type slipping, and failure by shear banding. The response to $[001]$ loading is softer, triggers work hardening, and failure by kinking and layer delamination. Furthermore, W_2AlB_2 able to retard fracture via ripplocations and twinning from 300 up to 1200 K.

Keywords: MAB phase; Machine-learning interatomic potentials; Mechanical properties; Molecular dynamics

1 Introduction

The swift development in the field of machine-learning interatomic potentials¹ (MLIPs) opens the door to molecular dynamics simulations (MD) of complex materials under experiment-relevant conditions, reaching near *ab initio* accuracy at greatly reduced computational costs^{2,3}. MLIPs are non-empirical models that learn atomic properties from a reference *ab initio* dataset, using mathematically convenient and possibly physically-motivated descriptors (e.g., moment tensors⁴, atomic clusters⁵) to encode atomic environments. MLIPs are improvable by active learning exploiting certain extrapolation control (e.g., the MaxVol grade via the D-optimality criterion⁶). However, fundamental challenges—such as (i) construction of robust and transferable training sets, and (ii) validation of MLIP-MD simulations beyond *ab initio* length scales—make efficient MLIP training for structurally and/or chemically complex materials and defects difficult. Especially MLIPs for simulations including wide range of mechanical strains and strain-activated defects are non-trivial, and we attempt making a step forward in

this direction.

Already MLIP development for elastic constants calculations is far from routine^{7,8}. Modelling nucleation and dynamics of defects governing macroscopic mechanical behaviour poses even bigger challenges^{9,10}, as extended defects are typically too large to be explicitly labelled by *ab initio* calculations and included in the training database. Examples of MLIPs tailor-trained for accurate simulations of dislocations¹¹ and grain boundaries^{12,13} most often concern elemental metals. MLIP-MD mechanistic simulations at the nanoscale have been sparse; including tensile testing and fracture toughness predictions for C-based materials^{9,14–16}, $BaZrO_3$ ¹⁷, TiB_2 ¹⁸, as well as nanoindentation simulations for W¹⁹, Si, AlN, SiC, and BC_2N ²⁰. Routine predictions of strength and toughness related quantities and mechanisms, however, have been hindered by the lack of MLIPs for structurally complex materials (e.g., multicomponent alloys, superlattices) and/or their unproved transferability (especially in case of universal pre-trained potentials such as M3GNET²¹, CHGNET²², or MACE²³).

MAB phases²⁴ (MABs) alternate atomically-thin layers of ceramic-like transition metal boride, M–B, with

mono- or bi-layers of an A-element (A=Al, Si, Ga, In, . . .). The modulated charge density distribution, with predominantly covalent–ionic bonds separated by metallic bonds, renders a combination of properties typical for ceramics (e.g., high-temperature strength and oxidation resistance) as well as for metals (e.g., high fracture toughness and damage tolerance). Thus, MABs are attractive for high-temperature structural applications, as protective coatings, sensors, low friction surfaces, electrical contacts, tunable damping films for microelectromechanical systems, or as a basis of 2D materials for new-generation nanodevices^{25–28}. With typical formula $M_{n+1}AB_{2n}$ ($n = 1, 2, 3, \dots$), MABs are rich in structures, chemistry, and bonding motifs; including five experimentally known hexagonal or orthorhombic phase prototypes: MAB (222 type, $Cmcm$ ²⁹), M_2AB_2 (212 type, $Cmmm$ ³⁰ and $P\bar{6}m2$ ²⁶), M_3AB_4 (314 type, $Pmmm$ ³¹), M_4AB_6 (416 type, $Cmmm$ ³²), and other stable phases predicted by *ab initio* calculations^{33–35}. The vast chemical and phase space together with numerous competing phases makes systematic screening of this material class difficult and results in relatively few MABs synthesised till today (Ti_2InB_2 ²⁶, Cr_2AlB_2 ^{31,32,36}, Cr_3AlB_4 ^{31,32}, Cr_4AlB_6 ³², $MoAlB$ ^{29,37–40}, $WAIB$ ^{29,41}, Fe_2AlB_2 ⁴², Mn_2AlB_2 ³⁰).

Mechanical response of MABs has been investigated by 0 K density functional theory (DFT) calculations including phenomenological descriptors of strength and ductility^{34,43–45}, toughness and damage tolerance^{46,47}. Experimental studies concerned indentation hardness (e.g., $MoAlB$ ^{38,39}, Mn_2AlB_2 ³⁰) and fracture toughness measurements (Fe_2AlB_2 ⁴⁸), as well as crack deflection and crack healing ($MoAlB$ ^{49,50}, Fe_2AlB_2 ⁵¹). Currently lacking atomistic simulations could help understanding how mechanical properties and atomic-scale deformation mechanisms of MABs depend on their chemistry and structure. They could also provide hints for a very fundamental question regarding deformation mechanisms; namely, whether MABs can nucleate so-called *ripplocations*⁵². Rippllocations are atomic layer ripples claimed to be the universal deformation mechanism in layered materials upon edge-on basal plane compression, observed at nm-to-km length scales (in MAX phases as well as geological formations)⁵³. Despite the laminated character of MABs and their similarity to MAX phases, no rippllocations have been reported, Chen *et al.*³⁷ even suggested that MABs *do not* rippllocate.

In this study, we present a systematic screening of 222, 212, and 314 type MABs containing group 4–6 transition metals, $M=(Ti, Ta, W)$, and $A=Al$, focusing on structural parameters, mechanical strength, tough-

ness, and fracture mechanisms as a function of temperature. The chosen MABs have been shown dynamically stable³⁴, some are isoelectronic to already synthesised MABs^{31,32,36}, and WAIB is experimentally known^{29,41}. Our results are derived from MD simulations with own MLIPs, validated in terms of lattice and elastic constants at $T \in \{0, 300, 1200\}$ K, as well as via extrapolation grade and energy (force, stress) analysis against $\approx 3 \cdot 10^6$ *ab initio* MD snapshots from finite-temperature mechanical tests. Uniaxial tensile simulations at the nanoscale ($\approx 300,000$ -atom supercells) serve for quantitative predictions of theoretical strength and toughness as a function of T . Furthermore, we elucidate deformation mechanisms—including rippllocations—and crack nucleation patterns characteristic for group 4–6 transition metal based MABs.

2 Methods

2.1 Ab initio dataset

Zero Kelvin *ab initio* and finite-temperature Born-Oppenheimer *ab initio* MD calculations were performed employing the VASP⁵⁴ code together with the projector augmented wave (PAW)⁵⁵ method and the Perdew-Burke-Ernzerhof exchange-correlation functional⁵⁶. The plane-wave cut-off energy was 300 eV, the reciprocal space was sampled with a single Γ -point, and the time step was always 1 fs. Considering $M=(Ti, Ta, W)$ and $A=Al$, models of the 222 ($M_2A_2B_2$ or simply MAB), 212 (M_2AB_2), and 314 (M_3AB_4) type MABs were based on the orthorhombic $Pmm2$, $Cmcm$, and $Pmmm$ structures²⁴, with the $x \parallel [100]$, $y \parallel [010]$, and $z \parallel [001]$. Calculations for 222, 212, and 314 type MABs were performed in 864-, 720-, 576-atom supercells ($6 \times 6 \times 2$), respectively, equilibrated at $T \in \{300, 1200\}$ K during (i) an isobaric-isothermal (NPT) simulation with Parrinello-Rahman barostat⁵⁷ and Langevin thermostat (with a 1 fs timestep, for at least 6 ps), followed by (ii) a simulation with the canonical (NVT) ensemble and the Nosé-Hoover thermostat (with a 1 fs timestep, for 2 ps), using time-averaged lattice parameters from the last two 2 ps of step (i).

To generate training and validation data for MLIPs (targeted to finite-temperature tensile simulations for single-crystal MABs), series of tensile tests were performed for each phase prototype and elemental combination at 300 and 1200 K. Specifically, uniaxial strain was applied in the [001], [010], and [001] direction, respectively, with a 2% strain step (including 3 ps NVT relaxation) until material’s fracture. The simulations followed Refs.^{58–60}. Additionally, shearing along the [100](010) and [100](001) slip systems and volumetric compression

were simulated at 1200 K, always starting from equilibrated structures. Shearing followed the setup of the above tensile tests, whereas volumetric compression was modelled via shrinking lattice parameters (a , b , c) by up to 5% and maintaining for 3 ps under the NVT ensemble. Furthermore, shock uniaxial tension was simulated by elongating the a (b , c) lattice parameter by 125–150%, initializing atoms at ideal lattice sites, and equilibrating for 3 ps under the NVT ensemble. Environments produced by such simulations were suggested useful for describing the onset of fracture during nanoscale tensile tests¹⁸.

2.2 Machine-learning interatomic potentials (MLIPs)

All MLIPs were trained in the moment tensor potential (MTP⁶¹) formalism using the `mliip-2`⁶ package with 16g MTPs, 5.5 Å cut-off radius, 1500 iterations of the Broyden-Fletcher-Goldfarb-Shanno algorithm⁶², and $\{1;0.01;0.01\}$ weights for energies, forces, stresses. MLIP(Ti-MABs), MLIP(Ta-MABs), and MLIP(W-MABs) were trained in an iterative active learning procedure, consistently with our previous work¹⁸. The split of *ab initio* MD data between randomly initialised training set (TS), learning set (LS), and validation set (VS) was 0.5%–79.5%–20%. Series of intermediate MLIPs were trained on configurations from a particular mechanical test, e.g., [010]-tensile loading of Ta₂AlB₂, and gradually merged/up-fitted until providing *accurate* extrapolation on all configurations in the LS, as indicated by the extrapolation grade ($\gamma < 2$; consistent with Refs.^{3,18,63}).

2.3 Molecular dynamics simulations

MD simulations employed the LAMMPS code⁶⁴ interfaced with the `mliip-2` package⁶. Computational setups consistent with the above described *ab initio* MD calculations was used for validation. Molecular statics was performed when comparing against 0 K *ab initio* data. Finite-temperature tensile test were conducted in $\approx 300,000$ -atom supercells with dimension of 15^3 nm³, and $x \parallel [100]$, $y \parallel [010]$, $z \parallel [001]$ (convergence of lattice parameters and stress/strain curves was tested in 10^3 to 10^5 -atom supercells). All MABs were equilibrated for 20 ps (1 fs time step) at the targeted temperature under the isobaric-isothermal (NPT) ensemble coupled to the Nosé-Hoover thermostat. Uniaxial tensile strain was applied along the [100], [010] or [001] direction, respectively, with a constant strain rate (50 Å/s), accounting for the Poisson's contraction (via NPT).

3 Results and discussion

3.1 Atomic-scale simulations

To screen structural and mechanical properties of group 4–6 transition metal based MABs—with M=(Ti, Ta, W), A=Al, and experimentally known orthorhombic 222, 212, and 314 type structures—we developed three MLIPs: MLIP(Ti-MABs), MLIP(Ta-MABs), and MLIP(W-MABs). First, they are employed for atomic-scale simulations concerning lattice and elastic constants as well as various mechanical tests, and validated against DFT/*ab initio* MD data at temperatures $T \in \{0, 300, 1200\}$ K.

Fig. 1 exemplifies atomic environments in our training sets, including stacking faults, distorted and/or intermixed layers, voids, and surfaces. These result from uniaxial/volumetric/shear strain in finite-temperature *ab initio* MD, i.e., were not hand-crafted using any material-specific knowledge. Consistently with the underlying *ab initio* calculations, training and validation errors of energies, forces, and stresses, quantified by the mean square error (RMSE), are below 3 meV/at., 0.14 eV/Å, and 0.2 GPa for MLIP(Ti-MABs); 20 meV/at., 0.20 eV/Å, and 0.3 GPa for MLIP(Ta-MABs); and 9 meV/at., 0.23 eV/Å, and 0.7 GPa for MLIP(W-MABs). Note that our validation set did not contain binary or other non-MAB compounds, as transferability to these was not targeted and up-fitting using own *ab initio* MD dataset for TiB₂ (TaB₂, WB₂) has slightly decreased accuracy for MABs.

In line with previous DFT phonon calculations³⁴, both *ab initio* MD and MLIP-MD indicate dynamical stability of the nine studied MABs (as time-averaged atomic vibrations in $\approx 10^3$ -atom supercells, at $T \in \{300, 1200\}$ K, remain near ideal sites). Thus, besides the experimentally known WAIB^{29,41}, also the other systems are at least metastable, though their formation may strongly depend on competing phases³⁵ and kinetics of the synthesis process.

Tab. 1 lists structural and elastic properties predicted at $T \in \{0, 300, 1200\}$ K. Differences between MLIP MD and DFT/*ab initio* MD in terms of lattice parameters and equilibrium volumes are small, reaching $(0.19 \pm 0.2)\%$. MLIP predictions may be in fact more accurate as the corresponding (time-averaged) stress tensor components are closer to zero, i.e., to the ideal equilibrium at given T . Irrespective of M element, the 314 phase exhibits the lowest volume, followed by the 212 and 222 type MABs. Note that the 314, 212, and 222 phase were indicated as the energetically most favourable MABs for M=Ti, M=Ta, and M=W, respectively³⁴.

Furthermore, Tab. 1 shows temperature evolution of

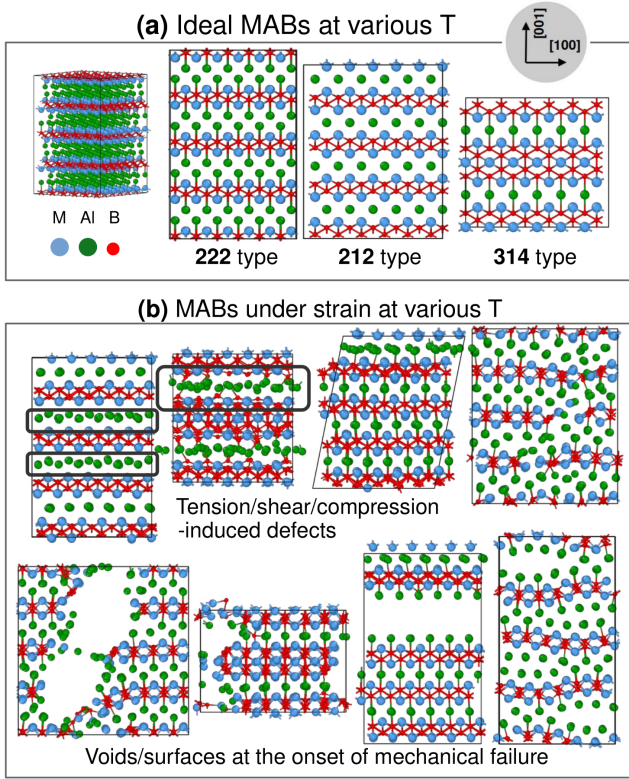


Figure 1. Illustration of atomic environments present in training sets of our MLIPs. (a) Ideal defect-free MABs with the 222, 212, and 314 type structure. The blue, green, and red spheres represent M=(Ti, Ta, W), A=Al, and boron, respectively. (b) MABs under various strain conditions, as extracted from finite-temperature *ab initio* MD mechanical tests. All supercells have $\approx 10^3$ atoms ($\approx 2^3 \text{ nm}^3$).

elastic constants, C_{ij} (computed from second-order polynomial fits of stress/strain data from tensile and shear tests). The comparison of MLIP-predicted C_{11} , C_{22} , and C_{33} —approximating directional Young’s moduli $E_{[100]}$, $E_{[010]}$, and $E_{[001]}$ —with own DFT/*ab initio* MD values yields $(7 \pm 5)\%$ difference. Calculations of the full elastic tensor (9 independent C_{ij} s⁶⁵) for selected MABs and temperatures indicate similar agreement for the remaining C_{ij} s. While MLIPs trained particularly for C_{ij} predictions can achieve higher accuracy (e.g., MLIPs for β -TiNbZr⁶⁶, bcc-TiZrHfTa⁸, or fcc-TiAlN⁷), presumably more transferable MLIPs—applicable to simulations with high strains and/or multiple phase structures—yield differences from DFT/*ab initio* MD similar to ours, e.g., $\Delta_{\text{DFT}}(C_{ij}) \approx 5\%$ for TiB₂¹⁸ or $\Delta_{\text{DFT}}(C_{ij}) = 0\text{--}25\%$ for W⁶⁷. The obtained differences from corresponding DFT/*ab initio* MD values are also well within the range of differences between 0 K C_{ij} s for the same MAB phase from various DFT studies (c.f. Refs.^{34,43,46} for MoAlB).

As expected, C_{ij} s of all MABs soften with T . Irre-

spective of T , all MABs are predicted to be elastically stiffer in-plane, parallel to M–B/A layers, compared to out-of-plane, orthogonal to M–B/A layers. With some exceptions (e.g., C_{22} of Ta-MABs), C_{11} , C_{22} , and C_{33} increase when changing 222→212→314 type phase, indicating increasing resistance to strains along main crystallographic directions.

Considering targeted predictions of theoretical tensile strength, toughness, and deformation mechanisms, our MLIPs are further validated against snapshots from finite-temperature mechanical tests, comprising total of $\approx 3 \cdot 10^6$ *ab initio* MD configurations (Fig. 2). In particular, (i) uniaxial [001], [010], and [100] tensile deformation, (ii) [100](010) and [100](001) shear deformation, and (iii) volumetric compression are simulated at 300 K and/or at 1200 K for each MAB phase. As supercells sizes affordable in *ab initio* MD (here $\approx 10^3$ -atom supercells; $\approx 2^3 \text{ nm}^3$) severely constrain nucleation of extended defects, we focus on showing consistency between MLIP and *ab initio* MD data, omitting discussion of the predicted mechanical properties.

Quantitative agreement between MLIP and *ab initio* MD mechanistic simulations is shown by closely overlapping stress/strain curves (Fig. 2a: example of room-temperature tensile test for Ti₂AlB₂) and the same/similar stress release mechanisms (e.g., layer bending and delamination). Note that due to finite-temperature effects, these stress release mechanisms may be activated slightly earlier/later in MLIP-MD (Fig. 2a: example of local stress drop at $\epsilon = 0.14$ and $\epsilon = 0.16$ during MLIP-MD and *ab initio* MD, respectively). Evaluation of extrapolation grades (Fig. 2b: example of room-temperature tensile test for Ti₂AlB₂) indicates interpolation ($\gamma \leq 1$) or accurate extrapolation ($\gamma < 2$; in line with Refs.^{3,18,63}), consistent with low statistical errors of MLIP-predicted energies, forces, and stresses (Fig. 2b: example of room-temperature tensile test for Ti₂AlB₂).

Extensive validation of the the here-developed MLIPs (Fig. 2f–q) supports their transferability to mechanical—especially tensile—simulations for single-crystal MAB phases. Importantly, no bias is shown with respect to certain phase, temperature, or loading condition (Fig. 2f–q). Extrapolation grades underscore accurate extrapolation during all mechanical tests (Fig. 2f,j,n: $\gamma \leq 1.5$) and the maximum stress error is < 2 GPa (Fig. 2i,m,q). Validation against compression tests (with up to 5% compression) indicates that our MLIPs can capture environments with small-to-medium compressive stresses, which may be relevant for Poisson’s contraction during our targeted nanoscale tensile simulations.

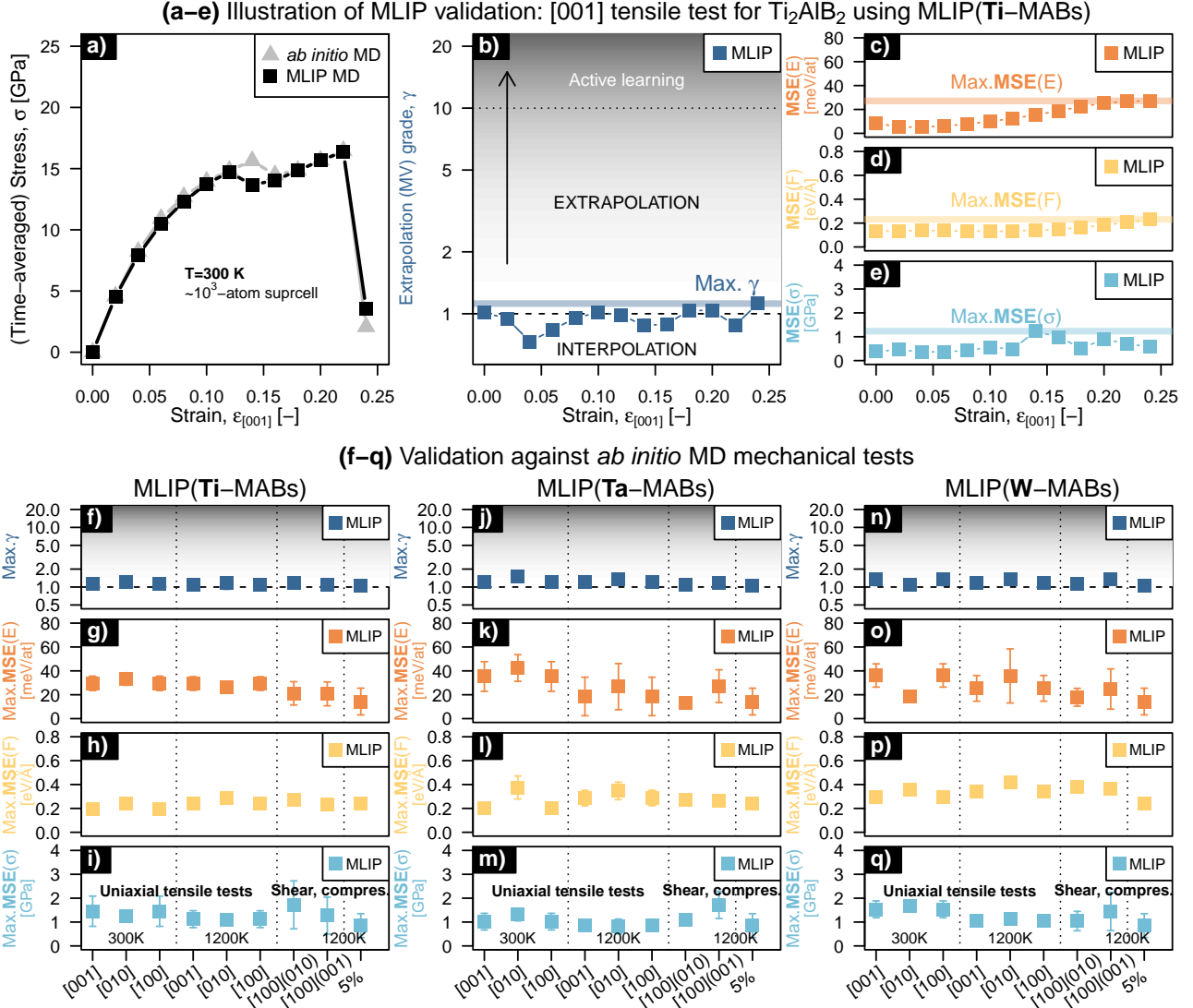


Figure 2. Validation of here-developed MLIPs against *ab initio* MD mechanical tests. Total of 54 atomic-scale mechanical tests (see the Methods) was simulated for the nine studied MABs with the orthorhombic 222, 212, and 314 type structures (listed in Tab. 1). (a) Comparison of MLIP-MD and *ab initio* MD stress/strain curves for Ti_2AlB_2 during [001] tensile loading at 300 K. (b) Evolution of the corresponding extrapolation grades, γ , where $\gamma \leq 1$ ($\gamma > 1$) indicates interpolation (extrapolation). Residual mean square errors, RMSEs, of MLIP-predicted (a) energies, E ; (b) forces, F ; and (c) stresses, σ ; evaluated for all configurations from *ab initio* MD (2700 configurations at each strain step). The horizontal lines in (b–e) guide the eye for the maximum γ , $\text{Max.}\gamma$; and the maximum RMSEs, $\text{Max.}\text{RMSE}(E)$, $\text{Max.}\text{RMSE}(F)$, and $\text{Max.}\text{RMSE}(\sigma)$; reached during the tensile test. Analogically obtained $\text{Max.}\gamma$, $\text{Max.}\text{RMSE}(E)$, $\text{Max.}\text{RMSE}(F)$, and $\text{Max.}\text{RMSE}(\sigma)$ are shown for various mechanical tests—uniaxial [001], [010], and [100] tensile deformation at 300 and 1200 K; [100](010) and [100](001) shear deformation at 1200 K; and 5% volumetric compression at 1200 K—for all (f–i) Ti-based, (j–m) Ta-based, and (n–q) W-based MABs. Note that data in panels (f–q) is derived from validation against $\approx 3 \cdot 10^6$ snapshots from *ab initio* MD calculations.

Table 1. Structural and elastic properties of the nine studied MABs predicted by MLIP(Ti-MABs), MLIP(Ta-MABs), and MLIP(W-MABs). The orthorhombic 222 (M₁AB), 212 (M₂AB₂), and 314 (M₃AB₄) type MABs, with A=Al, were modelled using $\approx 10^3$ -atom supercells (see the Methods). MLIP-predicted lattice parameters (a, b, c) and per-atom volumes (V) are shown at $T \in \{0, 300, 1200\}$ K and their difference from similarly derived DFT/*ab initio* MD values is marked by $\Delta_{\text{ref-us}}$. Elastic constants, C_{ij} (evaluated from second-order polynomial fit of the stress/strain data from uniaxial tensile or shear test, using 0–6% strains with a 2%-step), are shown together with the polycrystalline bulk (B), shear (G), Young’s modulus (E), and Poisson’s ratio (ν). For C_{11}, C_{22} , and C_{33} , differences from similarly calculated DFT/*ab initio* MD values is marked by $\Delta_{\text{ref-us}}$.

M	MAB phase	Temp. T [K]	Lattice parameters [Å]				Volume [$\text{\AA}^3/\text{at.}$]		Elastic constants and moduli [GPa / unitless: ν]															
			a	b	c	$\Delta_{\text{ref-us}}$ [%]	V	$\Delta_{\text{ref-us}}$ [%]	C_{11}	C_{22}	C_{33}	$\Delta_{\text{ref-us}}$ [%]	C_{12}	C_{23}	C_{23}	C_{44}	C_{55}	C_{66}	B	G	E	ν		
Ti	222	0	3.283	3.049	14.648	{0.0,0.1,0.2}	12.2	0.1	315	245	245	{1.4,4.9,9.8}	70	81	92	120	133	164	143	117	275	0.18		
			3.297 ⁴³	3.049 ⁴³	14.641 ⁴³		12.3 ⁴³		352 ⁴³	273 ⁴³	202 ⁴³		74 ⁴³	83 ⁴³	92 ⁴³	122 ⁴³	130 ⁴³	158 ⁴³	145 ⁴³	116 ⁴³	274 ⁴³	0.18 ⁴³		
			3.281 ³⁴	3.056 ³⁴	14.691 ³⁴		12.3 ³⁴		350 ³⁴	263 ³⁴	191 ³⁴		76 ³⁴	81 ³⁴	99 ³⁴	119 ³⁴	130 ³⁴	139 ³⁴	143 ³⁴	109 ³⁴	261 ³⁴	0.20 ³⁴		
		300		3.296	3.058	14.687	{1.0,0.2,0.8}	12.3	0.0	304	235	190	{2.5,3.1,12.8}	71	82	102	153	129	113	136	104	248	0.19	
				3.329	3.090	14.880	{0.0,0.0,0.2}	12.8	0.2	273	199	127	{2.7,1.8,5.3}	70	73	82	125	102	93	112	81	195	0.21	
	212	0		3.050	3.295	11.298	{0.0,0.2,0.0}	11.4	0.2	470	340	305	{3.6,1.3,11.7}	98	86	127	209	196	223	241	150	371	0.18	
				3.046 ⁴³	3.308 ⁴³	11.320 ⁴³		11.4 ⁴³		406 ⁴³	307 ⁴³	270 ⁴³		91 ⁴³	80 ⁴³	108 ⁴³	176 ⁴³	165 ⁴³	204 ⁴³	170 ⁴³	150 ⁴³	347 ⁴³	0.16 ⁴³	
				3.049 ³⁴	3.309 ³⁴	11.327 ³⁴		12.4 ³⁴		403 ³⁴	308 ³⁴	266 ³⁴		92 ³⁴	80 ³⁴	107 ³⁴	171 ³⁴	164 ³⁴	204 ³⁴	169 ³⁴	148 ³⁴	344 ³⁴	0.16 ³⁴	
		300		3.057	3.306	11.342	{0.0,0.1,0.1}	11.5	0.0	375	296	238	{3.5,1.5,3.3}	88	81	118	166	161	185	163	136	320	0.17	
				3.084	3.335	11.466	{-0.1,0.1,0.0}	11.8	0.0	328	259	189	{3.9,4.3,0.3}	88	80	100	139	137	156	143	113	268	0.19	
314	0		3.039	3.274	8.256	{0.0,0.2,0.1}	10.3	0.1	470	340	305	{17.6,13.0,2.4}	98	86	127	209	340	305	191	171	396	0.16		
			3.044	3.287	8.282	{0.0,0.1,0.2}	10.4	0.1	448	332	286	{2.6,3.7,9.4}	90	81	116	198	186	213	181	165	379	0.15		
			3.066	3.317	8.362	{0.1,0.1,-0.1}	10.6	0.1	410	315	244	{3.7,7.8,7.2}	93	85	117	172	160	198	171	142	334	0.17		
Ta	222	0	3.328	3.106	14.592	{0.5,0.0,0.3}	12.6	0.1	331	288	272	{15.4,13.0,2.4}	128	169	154	173	174	164	198	120	300	0.25		
			3.351 ⁴³	3.107 ⁴³	14.576 ⁴³		12.6 ⁴³		369 ⁴³	321 ⁴³	278 ⁴³		131 ⁴³	116 ⁴³	138 ⁴³	187 ⁴³	163 ⁴³	181 ⁴³	192 ⁴³	138 ⁴³	333 ⁴³	0.21 ⁴³		
			3.336 ³⁴	3.107 ³⁴	14.662 ³⁴		12.7 ³⁴		354 ³⁴	289 ³⁴	271 ³⁴		140 ³⁴	119 ³⁴	183 ³⁴	183 ³⁴	163 ³⁴	181 ³⁴	193 ³⁴	128 ³⁴	315 ³⁴	0.23 ³⁴		
		300		3.334	3.121	14.653	{0.3,0.3,0.1}	12.7	0.1	306	273	260	{11.2,10.1,3.4}	133	150	112	162	162	150	180	116	186	0.24	
				3.354	3.151	14.786	{0.2,0.3,0.0}	13.0	0.0	254	247	217	{8.6,11.6,5.0}	116	135	100	136	131	125	156	96	239	0.25	
	212	0		3.098	3.340	11.615	{0.7,0.1,0.9}	12.0	0.4	312	287	223	{2.3,2.5,5.8}	109	131	173	134	111	176	182	98	248	0.27	
				3.107	3.344	11.678	{0.3,0.3,0.1}	12.1	0.5	315	255	203	{9.1,2.2,1.5}	123	139	134	123	104	166	171	93	238	0.27	
				3.137	3.352	11.858	{0.2,0.1,0.2}	12.5	0.0	290	248	169	{2.3,0.8,14.4}	147	148	131	106	92	143	166	76	198	0.30	
	314	0		3.101	3.308	8.502	{0.2,0.2,0.2}	10.9	0.2	482	341	285	{0.5,14.4,11.7}	180	187	149	165	139	215	230	135	338	0.25	
				3.110	3.316	8.529	{0.1,0.3,0.4}	11.0	0.2	449	326	267	{2.7,11.4,4.1}	161	162	132	160	132	207	211	131	326	0.24	
				3.141	3.331	8.616	{0.2,0.1,0.2}	11.3	0.1	382	324	228	{6.6,3.6,11.2}	155	143	141	138	117	182	196	113	284	0.26	
W	222	0	3.207	3.121	13.943	{0.4,0.2,0.1}	11.6	0.1	378	333	389	{15.5,6.2,11.4}	203	133	144	194	206	159	229	144	356	0.24		
			3.217 ⁴³	3.118 ⁴³	13.985 ⁴³		11.7 ⁴³		405 ⁴³	365 ⁴³	349 ⁴³		189 ⁴³	143 ⁴³	160 ⁴³	183 ⁴³	195 ⁴³	171 ⁴³	233 ⁴³	145 ⁴³	361 ⁴³	0.24 ⁴³		
			3.223 ³⁴	3.122 ³⁴	13.990 ³⁴		11.7 ³⁴		396 ³⁴	385 ³⁴	356 ³⁴		183 ³⁴	142 ³⁴	155 ³⁴	181 ³⁴	196 ³⁴	170 ³⁴	229 ³⁴	146 ³⁴	361 ³⁴	0.24 ³⁴		
		300		3.218	3.128	13.953	{0.2,0.4,0.7}	11.7	0.0	357	339	342	{9.4,5.2,6.8}	196	118	143	188	153	188	215	136	337	0.24	
				3.207 ⁴¹	3.104 ⁴¹	13.924 ⁴¹		11.6 ⁴¹																
				3.238	3.147	14.147	{0.3,0.1,0.1}	12.0	0.1	334	329	334	{7.6,1.0,11.1}	195	129	154	148	160	128	203	109	277	0.25	
	212	0 K		3.081	3.140	11.505	{0.1,0.0,0.2}	11.1	0.2	556	494	370	{13.3,6.6,1.5}	196	158	194	176	170	234	275	169	422	0.24	
				3.088 ⁴³	3.139 ⁴³	11.566 ⁴³		11.2 ⁴³		511 ⁴³	474 ⁴³	365 ⁴³		187 ⁴³	154 ⁴³	179 ⁴³	147 ⁴³	115 ⁴³	163 ⁴³	262 ⁴³	139 ⁴³	354 ⁴³	0.28 ⁴³	
				3.089	3.149	11.545	{0.2,0.0,0.1}	11.2	0.1	487	458	334	{4.4,2.2,3.4}	175	148	183	166	162	221	251	156	388	0.24	
	314	0		3.104	3.173	11.666	{0.1,0.1,0.0}	11.5	0.0	398	374	264	{2.7,3.2,9.1}	166	147	148	147	142	193	213	127	319	0.25	
				3.079	3.161	8.390	{0.5,0.6,0.0}	10.2	1.1	498	322	342	{5.8,14.8,10.4}	174	142	149	170	167	200	228	148	364	0.23	
				3.085	3.174	8.418	{0.3,0.2,0.3}	10.3	0.2	490	377	361	{1.0,13.8,10.8}	212	185	192	155	163	180	265	138	351	0.27	
	1200		3.112	3.204	8.495	{0.1,0.1,0.1}	10.6	0.2	394	299	285	{6.7,14.5,3.9}	174	142	119	132	143	160	201	119	298	0.25		

3.2 Mechanical response of single-crystal MAB phases at the nanoscale

Validation of the here-developed MLIPs indicates that they can tackle various strain conditions far from elastic regime, particularly those relevant for tensile deformation. Employing these MLIPs, we simulate tensile tests for single-crystal MABs at length scales allowing for strain-induced nucleation of extended defects (Fig. 3). Specifically, the nine MABs previously modelled in $\approx 10^3$ -atom supercells are now represented by supercells with $\approx 300,000$ atoms ($\approx 15^3 \text{ nm}^3$). Although such simulations cannot be reproduced by *ab initio* MD, their reliability is indicated by (i) the MLIP's agreement with relevant atomic-scale *ab initio* MD calculations (Tab. 1, Fig. 2), (ii) negligible changes of size-independent material's properties (e.g., structural and elastic data from Tab. 1 remaining unchanged for supercells with 10^1 – 10^6 atoms), (iii) low extrapolation grades. The last mentioned can be evaluated also for nanoscale supercells under far-from-equilibrium conditions and indicate reliable extrapolation ($\gamma < 10$) of mechanical tests presented below.

Stress/strain curves derived from room-temperature tensile tests for the nine studied MABs (Fig. 3) show qualitatively different response to tensile loads parallel to M–B/A layers, i.e., along $[100] \parallel a$ and $[010] \parallel b$, and orthogonal to them, i.e., along $[001] \parallel c$. While the former is relatively stiff, the latter is initially softer and then exhibits strain hardening, hence resembling behaviour typical for metals. Strongly-directional mechanical response of MAB phases, suggested already by elastic constants calculations (Tab. 1, Refs.^{34,43,44}), therefore extends also beyond the linear-elastic regime. Qualitative differences between in-plane and out-of-plane mechanical behaviour are further underpinned by deformation mechanisms (see snapshots at fracture in Fig. 3). Specifically, in-plane tensile response is characterised by layer slipping, interpenetration, and crack nucleation diagonally across the layers or along the $[001]$ direction. Out-of-plane tensile loading causes layer bending and formation of kink bands followed by delamination.

Starting with **Ti-based MABs** (Fig. 3a–c, Tab. 2), three hypotheses can be drawn. (i) In-plane tensile strengths, $\sigma_{[100]}$ and $\sigma_{[010]}$, of any given phase prototype are very close and notably above $\sigma_{[001]}$; e.g., $\sigma_{[100]} \approx 28.0 \text{ GPa}$ of Ti_2AlB_2 is similar to $\sigma_{[010]} \approx 29.8 \text{ GPa}$ but significantly above $\sigma_{[001]} \approx 17.2 \text{ GPa}$. (ii) The strain at fracture, however, is higher subject to $[010]$ loading, rendering the highest toughness, $U_{[010]}$, in the $[010]$ direction; e.g., $U_{[010]} \approx 4.60 \text{ GPa}$ of Ti_2AlB_2 surpasses its $U_{[100]} \approx 2.34 \text{ GPa}$. (iii) Both ideal tensile strength

and toughness increase for $\text{TiAlB} \rightarrow \text{Ti}_2\text{AlB}_2 \rightarrow \text{Ti}_3\text{AlB}_4$, irrespective of the loading direction. This may seem intuitive for strength—mirroring the increased fraction of the harder ceramic material—but less for toughness. Examining structural changes at various deformation stages, we observe earlier layer bending, delamination, or layer interpenetration for TiAlB and Ti_2AlB_2 , in contrast with Ti_3AlB_4 , and their lower toughness may therefore originate from premature plasticity.

For **Ta-based MABs** (Fig. 3d–f, Tab. 2), MLIP-MD results render the following findings. (i) The $[010]$ direction is the hardest and the toughest: $\sigma_{[100]} > \sigma_{[010]} > \sigma_{[001]}$ (at variance with fairly basal-plane-isotropic Ti-MABs) and analogically for toughness. E.g., $\sigma_{[100]} \approx 29.7 \text{ GPa}$ of Ta_2AlB_2 exceeds its $\sigma_{[010]} \approx 19.7 \text{ GPa}$ as well as $\sigma_{[001]} \approx 13.7 \text{ GPa}$. (ii) Not only the $[001]$ but also the $[100]$ direction exhibits strain hardening, contrarily to Ti-MABs. Also stress/strain data for $[010]$ deformation indicate strain hardening, though less pronounced compared with the $[100]$ and $[010]$ loading conditions. Similarly to Ti-MABs, (iii) ideal tensile strength increases upon increasing the fraction of the ceramic-like component, i.e., for $\text{TaAlB} \rightarrow \text{Ta}_2\text{AlB}_2 \rightarrow \text{Ta}_3\text{AlB}_4$. The trend for toughness is almost like this, with the exception of $[100]$ and $[001]$ deformation during which Ta_2AlB_2 provides the highest toughness.

W-based MABs (Fig. 3g–i, Tab. 2) show fairly similar response to in-plane, $[100]$ and $[010]$, tensile strains, contrarily to Ta-MABs, but also Ti-MABs. Strain hardening is predicted subject to $[001]$ tensile loading, comparable to $M = \{\text{Ti}, \text{Ta}\}$. Noteworthy is the nucleation of twin boundaries in W_2AlB_2 (isoelectronic to the experimentally known Cr_2AlB_2 ^{31,32,36}) during $[001]$ tensile test, indicating superior resistance to crack initiation and propagation. The experimentally known WAlB does not particularly stand out, showing rather low strength ($\sigma \approx 11.6$ – 25.5 GPa) and moderate toughness ($U \approx 1.91$ – 2.50 GPa).

Among the studied MABs, Ti_3AlB_4 exhibits the highest theoretical tensile strength (Tab. 2: $\sigma_{[100]} \approx 37.3 \text{ GPa}$; $\sigma_{[010]} \approx 34.4 \text{ GPa}$), which is about 45 % below $[\bar{1}2\bar{1}0]$ tensile strength of a typical hard ceramic, TiB_2 ¹⁸. While Ti_3AlB_4 has not been synthesised, it has the lowest formation energy, E_f , among various mechanically and dynamically stable Ti-MABs (namely, E_f of Ti_2AlB_2 and TiAlB is 0.07 and 0.24 eV/at. higher, respectively)³⁴. Other MABs with high strength include Ti_2AlB_2 , Ta_3AlB_4 , and W_3AlB_4 .

The overall highest toughness is exhibited by Ta_3AlB_4 (Tab. 2: $U_{[010]} \approx 5.86 \text{ GPa}$), which is about 55 % above that of TiB_2 ¹⁸. Ta_3AlB_4 is energetically close to the

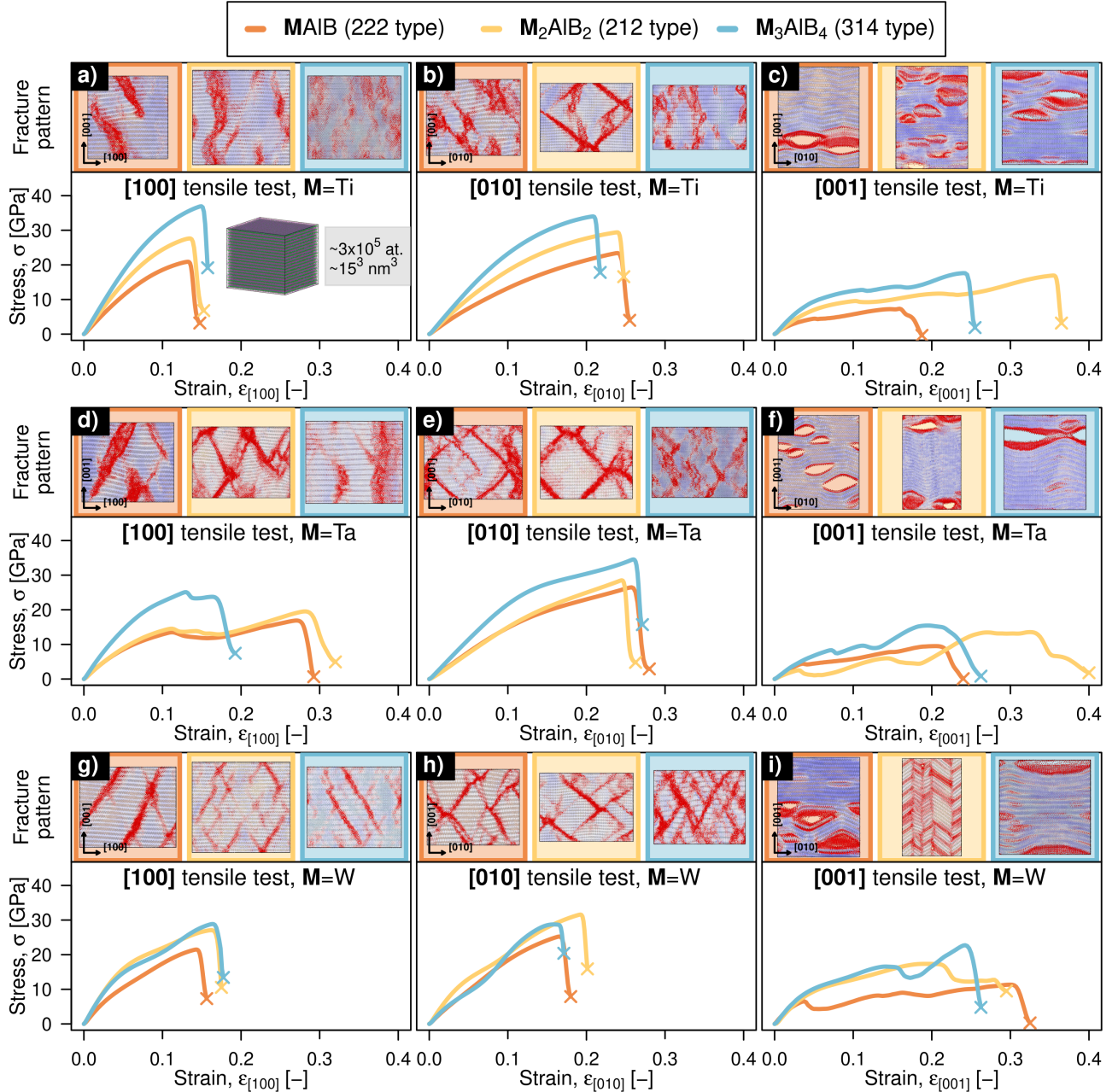


Figure 3. Stress/strain curves for the nine studied MABs, $M = (\text{Ti}, \text{Ta}, \text{W})$, $A = \text{Al}$, subject to uniaxial tensile deformation simulated by nanoscale MLIP-MD at 300 K. During each mechanical test, tensile strain (ϵ) was applied to initially defect-free supercells along the [100], [010], or [001] direction. The stress (σ) represents stress tensor component in the loaded direction (stresses normal to this direction are nullified due to Poisson's effect). Panels (a–c), (d–f), and (g–i) depict results for Ti-, Ta-, and W-based MABs. The orange, yellow, and blue line marks the 222, 212, and 314 type phase, respectively, each modelled by $\approx 300,000$ -atom supercell ($\approx 15^3 \text{ nm}^3$). Snapshots on the top of each panel illustrate fracture patterns, visualised by volumetric strain distribution (blue \rightarrow white \rightarrow red; with red denoting highly tensile-strained regions), where the frame colour marks the phase prototype. Note that determining exact fracture strains may be ambiguous and we only consider stress/strain data corresponding to reliable extrapolation grades ($\gamma < 10$).

ground-state Ta_2AlB_2 (0.01 eV/at. higher in E_f)³⁴. Note, however, that our toughness (U) expresses the energy consumed by the material until the global stress maxi-

um, not until the fracture point which may be ambiguous. Consequently, also W_2AlB_2 could possess superior toughness, as hinted by the structure snapshot at the on-

Table 2. Mechanical properties of the nine studied MABs, M= (Ti, Ta, W), A=Al, derived from nanoscale MLIP-MD simulations (Fig. 3). Theoretical tensile strengths— $\sigma_{[100]}^{\max}$, $\sigma_{[010]}^{\max}$, and $\sigma_{[001]}^{\max}$ —were evaluated as the maximum stress reached during the [100], [010], and [001] tensile test, respectively, where their mean value is denoted by $\bar{\sigma}^{\max}$ (shown together with standard deviation indicating the extent of anisotropy). Theoretical tensile toughness values— $U_{[100]}^{\max}$, $U_{[010]}^{\max}$, and $U_{[001]}^{\max}$ —were evaluated by integrating the corresponding stress/strain curve until the maximum stress point. The mean value is denoted by \bar{U} (shown together with standard deviation). As the supercells were initially defect-free, all values represent ideal upper bounds of strength and toughness attainable in single-crystal MABs with initially no defects.

M	MAB phase	Number of atoms	Temp. [K]	Theoretical tensile strength [GPa]				Theoretical tensile toughness [GPa]			
				$\sigma_{[100]}^{\max}$	$\sigma_{[010]}^{\max}$	$\sigma_{[001]}^{\max}$	$\bar{\sigma}^{\max}$	$U_{[100]}$	$U_{[010]}$	$U_{[001]}$	\bar{U}
Ti	222	243,000	300	21.3	23.6	7.7	17.5±8.6	1.79	3.42	0.82	2.00±1.30
	212	286,650	300	28.0	29.8	17.2	25.0±6.8	2.34	4.60	3.86	3.60±1.20
	314	294,914	300	37.3	34.4	17.8	29.9±10.5	3.47	4.59	2.92	3.70±0.90
Ta	222	243,000	300	17.2	26.7	9.6	17.8±8.5	3.19	4.16	1.26	2.90±1.50
	212	286,650	300	19.7	28.8	13.7	20.7±7.6	3.64	4.06	2.18	3.30±1.00
	314	294,914	300	25.5	34.9	15.6	25.3±9.7	2.85	5.86	1.76	3.49±2.12
W	222	243,000	300	21.9	25.5	11.6	19.7±7.2	1.91	2.50	2.37	2.30±0.30
	212	286,650	300	27.4	32.1	17.4	25.6±7.5	3.01	3.80	2.21	3.00±0.80
	314	294,914	300	29.3	29.1	23.0	27.1±3.6	3.02	2.51	3.31	2.90±0.40

set of fracture (Fig. 3i) showing nucleation of V-shaped defects, later identified as twin boundaries.

3.2.1 Response to in-plane tension: shear bands

Tensile loading parallel to basal planes induces layer slipping, typically along the $\{110\}\langle 001\rangle$ -type slip system, followed by nucleation of shear bands, most often diagonally across M–B/A layers. These phenomena—observed in all MABs—are exemplified by WAIB during room-temperature [010] tensile test (Fig. 4a). The high strain concentration localized along shear bands (blue→white→red colour code in Fig. 4a) causes nucleation of X-shaped defects and void opening inside the supercell (see local magnification in Fig. 4a3).

Mechanical failure by shear banding resembles behaviour of metals (e.g., Cu/Nb nanocomposites⁶⁸). Despite no configurations with shear bands were explicitly trained on, already atomic-scale *ab initio* MD tensile tests used to validate our MLIPs showed M–B/A layer slipping and intermixing (Fig. 4a4), thus supporting nanoscale predictions. Layer slipping and interpenetration is qualitatively similar for all studied MABs (see local magnifications in Fig. 4b). The necessary activation strain, however, typically decreases during [100] tensile test compared with [010] tensile test, suggesting lower energetic costs of (110)[100] slip (Fig. 4c). This effect is very pronounced for Ti-based MABs and gets less striking for their W-containing counterparts.

TaAIB and Ta₂AIB₂ are exceptions: postponing the onset of (011)[100] slip during [100] tensile test beyond the activation strain of (101)[010] slip during [010] loading. This is achieved via small bonding rearrangements (particularly tilting) within the ceramic-like M–B layers (Fig. 4d), mirrored by work strengthening (stress/strain

data in Fig. 3d). Contrarily to four and six valence electrons of Ti and W, the five valence electrons of Ta may be “just right” to activate these tiny rearrangements within the M–B network, hindering the onset of shear bands and fracture. In-depth understanding, however, would require careful bonding analysis.

3.2.2 Response to out-of-plane tension: Layer buckling, kink bands, and twins

Work hardening and high fracture strains shown in stress/strain curves for [001] tensile tests (Fig. 3c,f,i) suggest the ability to redistribute and relax accumulated stresses via plastic deformation. Subsequent structural analysis reveals that key nm-scale mechanisms characterising out-of-plane loading are M–B layer ripples, sliding, and buckling, or nucleation of ripplications and mechanical twins (Fig. 5).

Generally, [001] tensile strain first causes small layer ripples, nucleating uniformly throughout the lattice and resembling high-frequency small-amplitude, most often anti-phase waves (Fig. 5a1). These facilitate work hardening. Further [001] strain increase relaxes these ripples via M–A/B layer sliding (Fig. 5a2) and, subsequently, the layers start buckling similarly to low-frequency, most often in-phase waves (Fig. 5a3). As buckling becomes locally more pronounced, turning into irreversible kink boundaries, some layers delaminate (Fig. 5c), resulting in nanocrack growth approximately along (001) planes. This is consistent with *ab initio* MD tensile tests showing layer ripples, sliding, and delamination, followed by formation of approximate (001) surfaces (Fig. 5a4).

Differences between individual MABs lie in their more-or-less-strong ability to nucleate anti-phase M–A layer ripples and retard kinking-induced failure via uni-

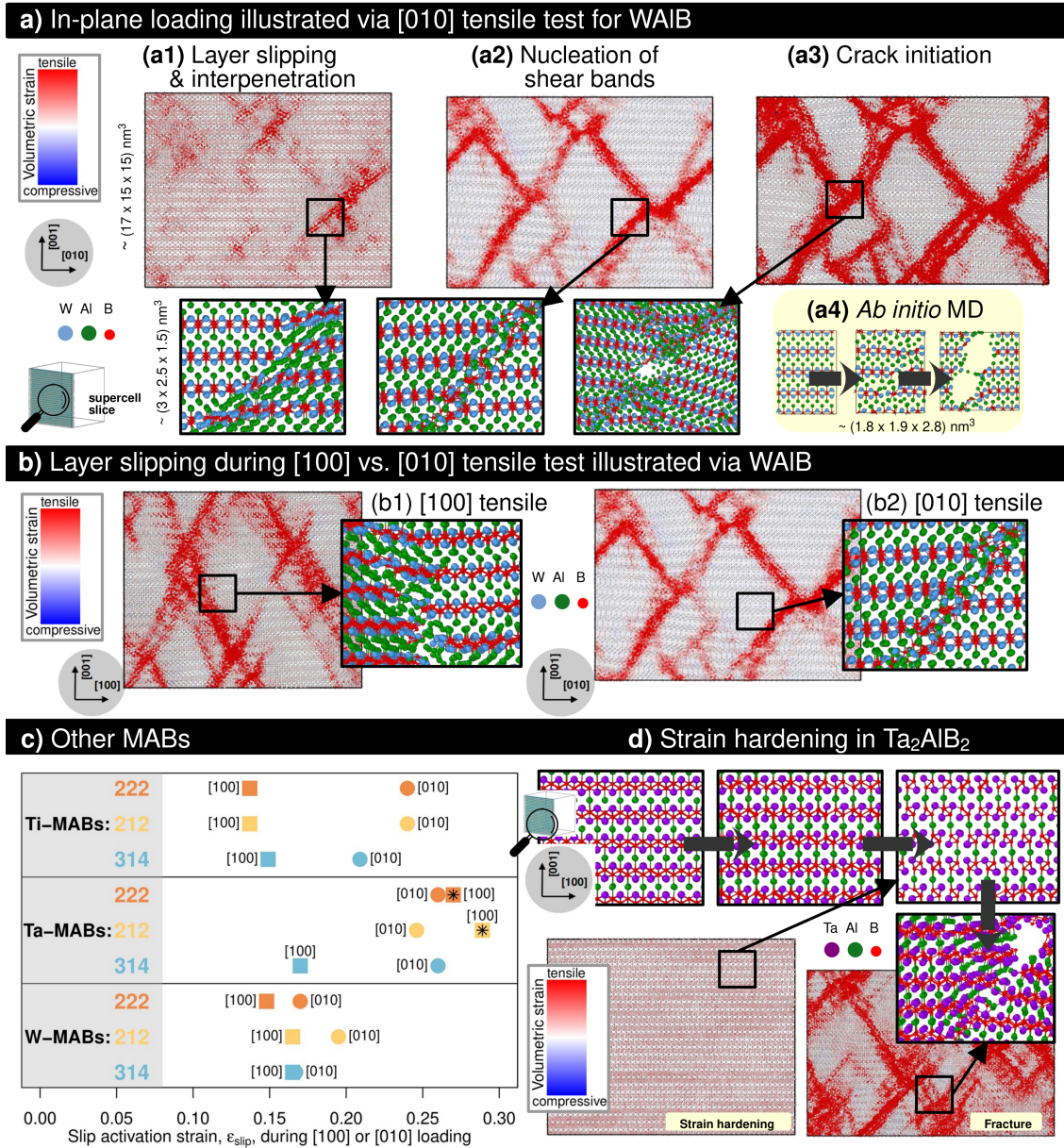


Figure 4. Deformation mechanisms of MAB phases during in-plane loading, derived from MLIP-MD room-temperature uniaxial tensile tests. (a) Typical strain-induced structural changes illustrated by WAIB (stress/strain data in Fig. 3h). The blue→white→red colouring mirrors distribution of the volumetric strain (compressive→zero→tensile) and highlights crack initiation patterns (red). The magnifying glass icon marks snapshots that are local magnifications of the supercell, typically $\approx (3 \times 3 \times 2) \text{ nm}^3$. (b) Layer slipping during [100] and [010] tensile tests illustrated by WAIB (stress/strain data in Fig. 3g–h). (c) Slip activation strain during [100] and [010] tensile tests (stress/strain data in Fig. 3), where the star for TaAlB and Ta₂AlB₂ indicates that these MABs exhibit strain hardening. (d) Illustration of strain hardening mechanism in Ta₂AlB₂ during [100] tensile test (stress/strain data in Fig. 3d).

form buckling or ripplocations (Fig. 5b). In line with atomic-scale *ab initio* MD, anti-phase layer ripples in nanoscale MLIP-MD simulations almost always nucleate along the [010] direction and are significantly less pronounced in 314 type MABs (Fig. 5b1), where they also live within shorter strain range (Fig. 5b2). This may

be intuited via higher strain/energetic costs of bending thicker ceramic-like layers of 314 type MABs. Generally, Al seems to act like a lubricant facilitating movements of the stiffer M–B sublattice. Ti₂AlB₂, Ta₂AlB₂, and WAIB exemplify MABs efficiently postponing the onset of kinking-induced mechanical failure by gradual layer

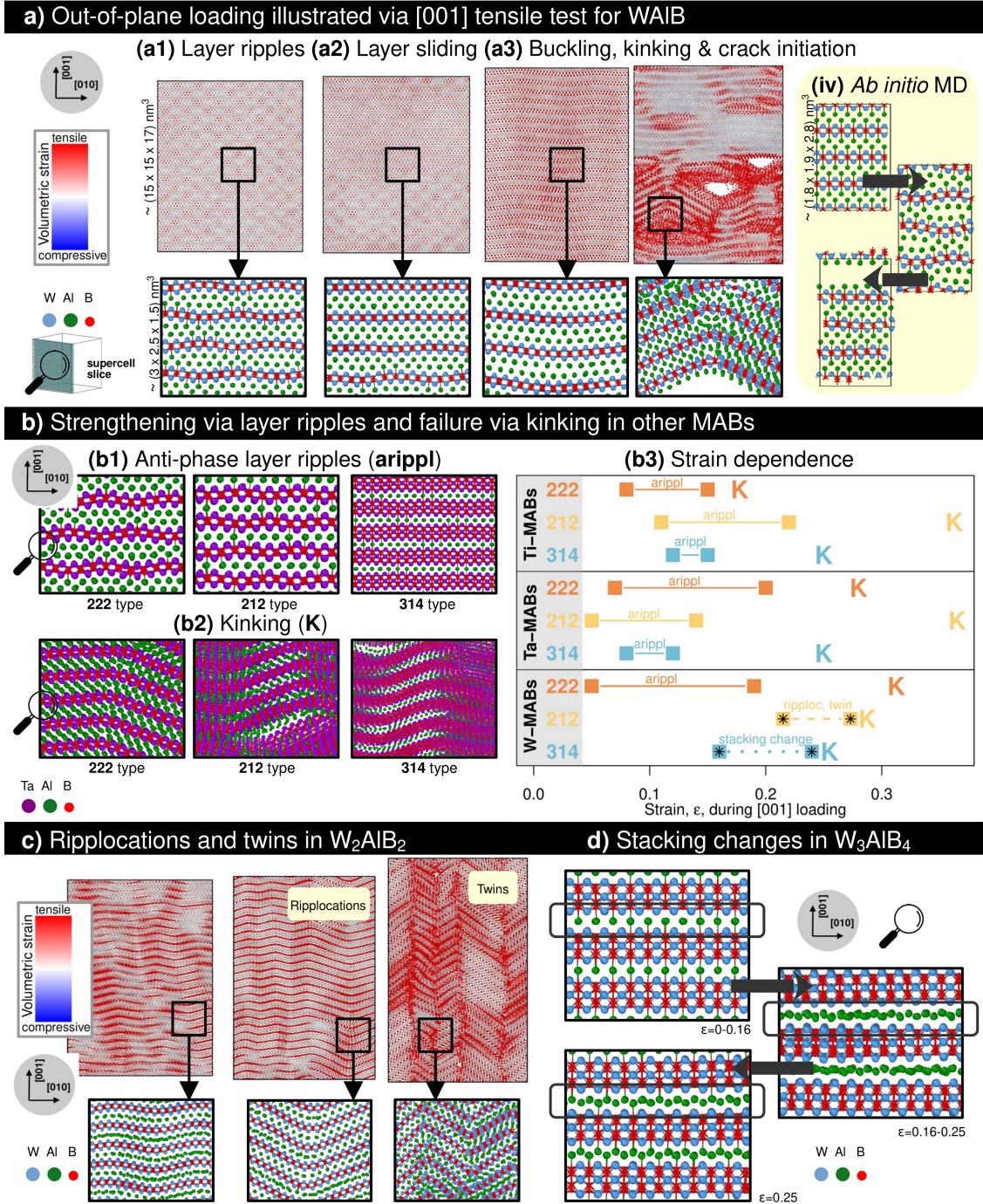


Figure 5. Deformation mechanisms of MAB phases during loading normal to basal planes, derived from MLIP-MD room-temperature uniaxial tensile tests. (a) Typical strain-induced structural changes illustrated by WAIB (stress/strain data in Fig. 3i). The blue→white→red colouring mirrors distribution of the volumetric strain (compressive→zero→tensile) and highlights crack initiation patterns (red). The magnifying glass icon marks snapshots that are local magnifications of the supercell, typically $\approx (3 \times 3 \times 2) \text{ nm}^3$. (b) Magnifications of layer ripples and kinks together with the corresponding strains for all MABs. (c) Snapshots of ripplings and twins in W_2AlB_2 . (d) Stacking faults in W_3AlB_4 .

buckling. Contrarily in $TiAlB$, these buckles almost immediately turn into irreversible kink boundaries, causing an early fracture.

W_2AlB_2 and W_3AlB_4 do not exhibit anti-phase layer ripples. Instead, the former deforms via ripplings and twinning (Fig. 5c), while the latter forms stacking

faults within Al layers (Fig. 5d). These (and other) stackings faults are observed in *ab initio* MD tensile tests for W_3AlB_4 as well as for other MABs, e.g., Ta_2AlB_2 and W_2AlB_2 (note, however, the 2% strain step, no Poisson’s contraction and severe size constraints of *ab initio* MD). At the nanoscale, stacking changes appear as a local by-product of M–B/A layer sliding but only in W_3AlB_4 , they form throughout nearly the entire supercell and live within fairly large strain range (Fig. 5b2). M–B/A layer sliding—accompanied by stacking changes in Al layers—is an important mechanism also for W_2AlB_2 where it mediates changes in the twinning angle, namely its decrease, mirrored by increasing strain concentration and, ultimately, void opening.

3.3 Temperature effects

Constituting M–B layers of MABs, transition metal borides belong to ultra-high temperature ceramics (UHTCs) with outstanding high-temperature stability (melting points 2500–3500 K), hardness, resistance to corrosion, abrasive and erosive wear⁶⁹. Here we compare mechanical response of MABs at room and elevated temperature, represented by 1200 K (chosen in view of our validation against *ab initio* MD data, Tab. 1, Fig. 2, and oxidation experiments for MABs^{38,49} at temperatures relevant for cutting tool applications).

Besides expectable temperature-driven decline in theoretical tensile strength and toughness, mechanical properties (Tab. 3) and deformation mechanisms (Fig. 6) at 1200 K remain consistent with those predicted at 300 K. This includes work hardening subject to [001] tensile tests and ripplocation activity of W_2AlB_2 . Exceptions are TaAlB and TiAlB losing the ability of work hardening during [100] loading (TaAlB) and gaining the ability to ripplocate during [001] loading (TiAlB). High-temperature mechanical response is generally characterised by larger atomic displacements, more frequent layer sliding, and (local) changes of the Al stacking sequence (similar to Fig. 5d). It is also less strength-anisotropic, especially due to $\sigma_{[100]}$ and $\sigma_{[010]}$ decreasing generally faster, by $(27 \pm 5)\%$, compared with $(14 \pm 9)\%$ decrease of $\sigma_{[001]}$, where standard deviations reflect values for all MABs.

A slight decline of [001] tensile strength and toughness is predicted for Ti_3AlB_4 , in which $\sigma_{[001]}$ and $U_{[001]}$ decrease by only a 2 and 5 %, respectively, as T rises from 300 to 1200 K (Tab. 3). Other examples of small temperature effects along [001] direction are Ta_2AlB_2 , Ta_3AlB_4 , and W_2AlB_2 yielding a $\sigma_{[001]}$ and $U_{[001]}$ decrease of 4–14% and 1–14 %, respectively. The experimentally known WAIB exhibits a fairly large drop of

both strength and toughness, although, again, less pronounced normal to basal planes (Fig. 6a): $\sigma_{[001]}$ and $U_{[001]}$ decline by 12 and 26 %, respectively, while $\sigma_{[100]}$ and $U_{[100]}$ decline by 32 and 45 %, respectively.

Temperature effects on ripplocation and twinning activities of W_2AlB_2 (Fig. 6b) are minimal, mirrored by $U_{[001]}$ decrease of 1% (Tab. 3). Additionally to simulations at $T \in \{300, 600, 900, 1200\}$ K, we tested various supercell sizes and included a free surface, all pointing towards nucleation of ripplocations and twins during [001] tensile loading. TiAlB presents similar ripplocation-based response to [001] strain within temperatures range 600–1200 K. This phase, however, may be difficult to synthesise (with E_f about 0.24 eV/at. above that of Ti_3AlB_4 ³⁴) and it is also overshadowed by W_2AlB_2 in terms of theoretical tensile strength and toughness in all directions.

3.4 Design implications

Among our most interesting predictions is the ability of W_2AlB_2 —with formation energy 0.02 eV/at. above that of the experimentally known WAIB³⁴—to form ripplocations, followed by nucleation of mechanical twins. Both ripplocations and twins are activated in a wide temperature range and are likely responsible for only minor toughness decrease from 300 up to 1200 K.

Generally, twins are known to enhance the hardness, toughness, thermal stability, as well as wear resistance of materials, however, their formation in ceramics is typically prohibited by high stacking-fault energies^{70,71}. The modulated ceramic-like/metallic-like bonding character of MABs may provide more favourable conditions for stacking faults, as indicated by both *ab initio* MD as well as MLIP-MD simulations for W_2AlB_2 but also for other MABs, e.g., TiAlB, Ta_2AlB_2 , W_3AlB_3 . Intuitively, low stacking fault energies may not be the only decisive factor for twinning in MABs. We speculate that twinning is related to the ability to ripplocate, based on simulations for W_2AlB_2 and TiAlB (above 300 K). Instead of highly-symmetric twin boundaries, other MABs nucleate kink boundaries, preceded by layer buckling which, however, seems too short and has too low angles to be called ripplocations.

How likely is detecting ripplocations or twins in W_2AlB_2 under real lab-scale conditions? In MAX phases—with atomically-laminated structures similar to MABs—ripplocations and twins have been reported during indentation tests comprising basal-plane compression^{53,72,73}. Although our loading is tensile, the $\approx 7\%$ in-plane Poisson compression at the onset of ripplocation activity could mimic regions near the indenter tip.

Table 3. High-temperature mechanical properties of the nine studied MABs, M=(Ti, Ta, W), A=Al, derived from nanoscale MLIP-MD simulations at 1200 K. Computational details were consistent with previous tensile tests at 300 K (Fig. 3) and the notation follows Tab. 2. Specifically, $\sigma_{[100]}^{\max}$ ($U_{[100]}^{\max}$), $\sigma_{[010]}^{\max}$ ($U_{[010]}^{\max}$), and $\sigma_{[001]}^{\max}$ ($U_{[001]}^{\max}$) denote theoretical tensile strength (toughness) in the [100], [010], and [001] direction, respectively. Percentages in brackets, [X%], show differences from the corresponding value at 300 K.

M	MAB phase	Number of atoms	Temp. [K] T	Theoretical tensile strength [GPa]				Theoretical tensile toughness [GPa]			
				$\sigma_{[100]}^{\max}$	$\sigma_{[010]}^{\max}$	$\sigma_{[001]}^{\max}$	$\bar{\sigma}^{\max}$	$U_{[100]}$	$U_{[010]}$	$U_{[001]}$	\bar{U}
Ti	222	243,000	1200	15.5	16.3	6.2	12.7±5.6	1.11	1.89	0.75	1.2±0.6
				[−27%]	[−31%]	[−19%]	[−27%]	[−38%]	[−45%]	[−9%]	[−40%]
	212	286,650	1200	21.3	22.3	13.2	18.9±5.0	1.73	2.96	2.91	2.50±0.70
Ti	314	294,914	1200	29.1	27.3	17.5	24.6±6.3	2.40	3.37	2.77	2.80±0.50
				[−22%]	[−22%]	[−2%]	[−18%]	[−31%]	[−27%]	[−5%]	[−24%]
Ta	222	243,000	1200	12.0	18.7	8.9	13.2±5	1.13	2.09	2.03	1.80±0.50
				[−30%]	[−30%]	[−7%]	[−26%]	[−65%]	[−50%]	[61%]	[−38%]
	212	286,650	1200	13.9	21.7	13.2	16.2±4.7	2.00	2.50	2.95	2.10±0.30
Ta	314	294,914	1200	21.2	26.5	14.2	20.7±6.2	2.08	3.23	2.00	2.40±0.70
				[−17%]	[−24%]	[−9%]	[−18%]	[−27%]	[−45%]	[+14%]	[−31%]
W	222	243,000	1200	14.8	16.3	10.2	13.8±3.2	1.05	1.16	1.76	1.30±0.40
				[−32%]	[−36%]	[−12%]	[−30%]	[−45%]	[−54%]	[−26%]	[−43%]
	212	286,650	1200	20.2	22.4	15.0	19.2±3.8	1.93	2.10	2.19	2.10±0.10
W	314	294,914	1200	21.1	23.1	15.5	19.9±3.9	1.94	2.02	2.97	2.30±0.60
				[−28%]	[−21%]	[−33%]	[−37%]	[−36%]	[−20%]	[−10%]	[−21%]

An important question for follow-up research concerns interactions between ripplocations and typical growth defects (e.g., vacancies, dislocations, grain boundaries) in W_2AlB_2 . In this regard, little is known for any material (see, e.g., studies of graphite showing that ripplocations migrate towards vacancies and annihilate⁷⁴).

Besides W_2AlB_2 , other promising MAB phase candidates include Ta_2AlB_2 and W_3AlB_4 —providing a suitable basis for high stacking fault density, thus, fine-tuning plasticity—or Ti_3AlB_4 providing the highest theoretical tensile strength. In view of [001]-tensile-strain-induced work hardening (predicted for all MABs) as well as ripplocation and twinning activities (W_2AlB_2 , $TiAlB$), it may be advantageous growing MABs with basal planes normal to the substrate, as e.g. Cr_2AlB_2 ³⁶. During nanoindentation, MABs with such preferential orientation could exhibit in-plane tensile stresses similar to the simulated ones, facilitating work hardening and superior fracture resistance.

4 Conclusions

Tensile response of the group 4–6 transition metal based single-crystal MAB phases—with M = (Ti, Ta, W), A = Al, and the 222, 212, and 314 type phases—was screened by nanoscale machine-learning powered molecular dynamics simulations, both at 300 K as well as at elevated temperatures. Key deformation/failure mechanisms included (i) slipping, the easiest along the

{110}<001> slip system, and shear-banding subject to in-plane tensile loads; (ii) layer buckling—mirrored by strain hardening—and kinking subject to loads normal to basal planes; (iii) ripplocations and twins nucleating in W_2AlB_2 .

Ab initio data set for active learning of our MLIPs was generated semi-automatically, with little material-specific knowledge; by simulating series of atomic-scale mechanical tests (< 10³-atom supercells, finite T) triggering growth of various defective environments (e.g., stacking faults, buckled or mixed layers, voids, surfaces). This strategy is likely transferable to other MABs. Validation concerned statistical errors of atomic properties evaluated against $\approx 3 \cdot 10^6$ DFT/*ab initio* MD configurations, predictions of observables, and extrapolation grade analysis.

Ti_3AlB_4 exhibited the highest theoretical tensile strength ($\approx 45\%$ of that for a typical hard ceramic, TiB_2 ¹⁸), whereas Ta_2AlB_2 , W_2AlB_2 , Ta_3AlB_4 , W_3AlB_4 showed outstanding toughness. Temperature effects were generally anisotropic: causing faster deterioration of mechanical properties in-plane, compared with mild effects along [001]. We suggest that Ta- and W-based MABs with the 212 or 314 phase are especially promising for experimental investigations including micromechanical testing and TEM studies. Ta_2AlB_2 and W_3AlB_4 are suitable for tuning transformation plasticity via stacking fault formation, while W_2AlB_2 allows for toughness enhancement via strain-activated ripplocations.

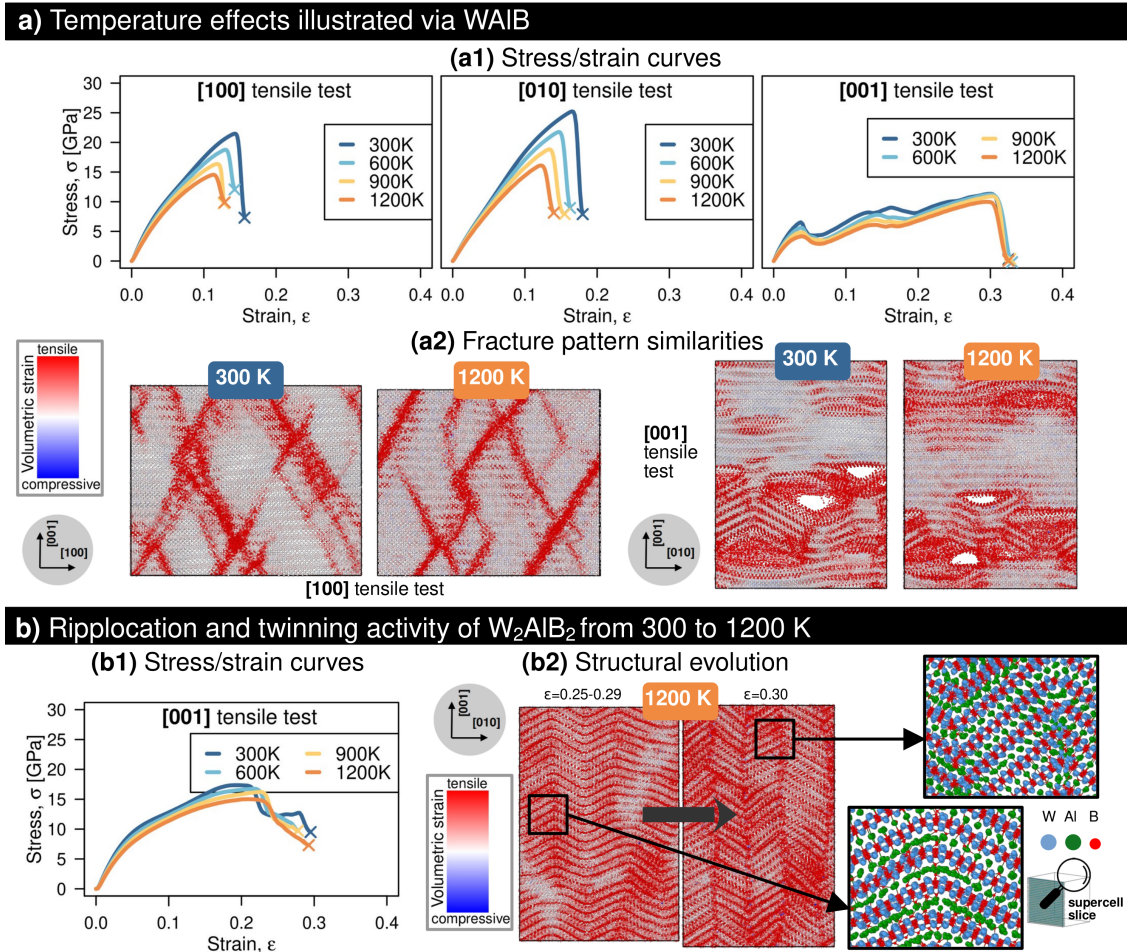


Figure 6. High-temperature mechanical response of MABs derived from nanoscale MLIP-MD simulations.

Computational details were consistent with previous tensile tests at 300 K (Fig. 3) (a) Typical T effects in stress/strain curves (showing more significant decrease subject to in-plane loading) and deformation mechanisms (remaining qualitatively unchanged), as illustrated by WAIB. (b) Negligible changes of ripplcation and twinning abilities of W_2AlB_2 .

The—nearly temperature-independent—ripplcation and twinning ability of W_2AlB_2 seems unique and may stem from its particular electronic structure, easy Al layer sliding, and energy landscape of certain stacking faults. These are proposed as important directions of follow-up research, together with interactions between ripplcations and typical growth defects, as well as the response of MABs to mechanical loads in the presence of a pre-crack. Enhancing the transferability of our MLIPs to such simulations will require active learning on under-represented environments, e.g., highly compressed, off-stoichiometric, and featuring planar defects.

We illustrated that MLIPs for complex material systems can be trained in semi-automatic fashion and used to predict temperature evolution of deformation-related descriptors, inherent strengthening mechanisms as well as nucleation of plasticity-enhancing defects at scales

accessible to experiment. Considering phase stability trends and other properties of MABs being mostly driven by the M element³⁴, our training sets may accelerate MLIP training for MABs of all group 4–6 transition metals and various A species.

CRedit authorship contribution statement

NK: Conceptualisation, Methodology, Investigation, Data curation, Visualisation, Writing – original draft. **SL:** Data curation, Validation, Writing – review & editing. **LH:** Resources, Writing – review & editing. **DGS:** Conceptualisation, Methodology, Resources, Writing – review & editing. **PHM:** Resources, Writing – review & editing.

Declaration of Competing Interests

The authors declare no competing interests.

Data Availability

The data presented in this study are available from the corresponding author upon reasonable request.

Acknowledgements

NK and PHM acknowledge the Austrian Science Fund, FWF, 10.55776/PAT4425523. LH acknowledges financial support from the Swedish Government Strategic Research Area in Materials Science on Functional Materials at Linköping University SFO-Mat-LiU No. 2009 00971 and the support from Knut and Alice Wallenberg Foundation Scholar Grant KAW2019.0290. DGS acknowledges financial support from the Swedish Research Council (VR) through Grant N° VR-2021-04426 and the Competence Center Functional Nanoscale Materials (FunMat-II) (Vinnova Grant No. 2022-03071). The computations handling were enabled by resources provided by the National Academic Infrastructure for Supercomputing in Sweden (NAISS) and the Swedish National Infrastructure for Computing (SNIC) at the National Supercomputer Center (NSC) partially funded by the Swedish Research Council through grant agreements no. 2022-06725 and no. 2018-05973, as well as by the Vienna Scientific Cluster (VSC) in Austria. The authors acknowledge TU Wien Bibliothek for financial support through its Open Access Funding Programme.

References

1. Mishin, Y. Machine-learning interatomic potentials for materials science. *Acta Materialia* **214**, 116980 (2021).
2. Smith, J. S., Isayev, O. & Roitberg, A. E. ANI-1: an extensible neural network potential with DFT accuracy at force field computational cost. *Chem. Sci.* **8**, 3192–3203 (2017).
3. Shapeev, A. V., Podryabinkin, E. V., Gubaev, K., Tasnádi, F. & Abrikosov, I. A. Elinvar effect in β -Ti simulated by on-the-fly trained moment tensor potential. *New J. Phys.* **22**, 113005 (2020).
4. Shapeev, A. V. Moment tensor potentials: A class of systematically improvable interatomic potentials. *Multiscale Model. Simul.* **14**, 1153–1173 (2016).
5. Drautz, R. Atomic cluster expansion for accurate and transferable interatomic potentials. *Phys. Rev. B* **99**, 014104 (2019).
6. Novikov, I. S., Gubaev, K., Podryabinkin, E. V. & Shapeev, A. V. The mlip package: moment tensor potentials with mpi and active learning. *Mach. learn.: sci. technol.* **2**, 025002 (2020).
7. Tasnádi, F., Bock, F., Tidholm, J., Shapeev, A. V. & Abrikosov, I. A. Efficient prediction of elastic properties of $\text{Ti}_{0.5}\text{Al}_{0.5}\text{N}$ at elevated temperature using machine learning interatomic potential. *Thin Solid Films* **737**, 138927 (2021).
8. Gubaev, K. *et al.* Finite-temperature interplay of structural stability, chemical complexity, and elastic properties of bcc multicomponent alloys from ab initio trained machine-learning potentials. *Phys. Rev. Mater.* **5**, 073801 (2021).
9. Mortazavi, B., Zhuang, X., Rabczuk, T. & Shapeev, A. V. Atomistic modeling of the mechanical properties: the rise of machine learning interatomic potentials. *Mater. Horizons* **10**, 1956–1968 (2023).
10. Deng, T. *et al.* Room-temperature exceptional plasticity in defective Bi_2Te_3 -based bulk thermoelectric crystals. *Science* **386**, 1112–1117 (2024).
11. Zhang, L., Csányi, G., van der Giessen, E. & Maresca, F. Efficiency, accuracy, and transferability of machine learning potentials: Application to dislocations and cracks in iron. *Acta Materialia* **270**, 119788 (2024).
12. Nishiyama, T., Seko, A. & Tanaka, I. Application of machine learning potentials to predict grain boundary properties in fcc elemental metals. *Phys. Rev. Mater.* **4**, 123607 (2020).
13. Ito, K., Yokoi, T., Hyodo, K. & Mori, H. Machine learning interatomic potential with DFT accuracy for general grain boundaries in α -Fe. *npj Comput. Mater.* **10**, 255 (2024).
14. Mortazavi, B. & Zhuang, X. Low and anisotropic tensile strength and thermal conductivity in the single-layer fullerene network predicted by machine-learning interatomic potentials. *Coatings* **12**, 1171 (2022).
15. Mortazavi, B. *et al.* First-principles multiscale modeling of mechanical properties in graphene/borophene heterostructures empowered by machine-learning interatomic potentials. *Adv. Mater.* **33**, 2102807 (2021).
16. Qamar, M., Mrovec, M., Lysogorskiy, Y., Bochkarev, A. & Drautz, R. Atomic cluster expansion for quantum-accurate large-scale simulations of carbon. *J. Chem. Theory Comput.* **19**, 5151–5167 (2023).
17. Wang, Z. *et al.* A machine-learning interatomic potential to understand the anisotropic fracture behavior of BaZrO_3 material. *Solid State Ionics* **401**, 116358 (2023).

18. Lin, S. *et al.* Machine-learning potentials for nanoscale simulations of tensile deformation and fracture in ceramics. *npj Comput. Mater.* **10**, 67 (2024).
19. Domínguez-Gutiérrez, F. J. *et al.* Nanoindentation of tungsten: From interatomic potentials to dislocation plasticity mechanisms. *Phys. Rev. Mater.* **7**, 043603 (2023).
20. Podryabinkin, E. V. *et al.* Nanohardness from first principles with active learning on atomic environments. *J. Chem. Theory Comput.* **18**, 1109–1121 (2022).
21. Chen, C. & Ong, S. P. A universal graph deep learning interatomic potential for the periodic table. *Nat. Comput. Sci.* **2**, 718–728 (2022).
22. Deng, B. *et al.* Chgnet as a pretrained universal neural network potential for charge-informed atomistic modelling. *Nat. Mach. Intell.* **5**, 1031–1041 (2023).
23. Batatia, I. *et al.* A foundation model for atomistic materials chemistry. *arXiv preprint arXiv:2401.00096* (2023).
24. Kota, S., Sokol, M. & Barsoum, M. W. A progress report on the MAB phases: atomically laminated, ternary transition metal borides. *Int. Mater. Rev.* **65**, 226–255 (2020).
25. Dahlqvist, M. *et al.* Theoretical prediction and synthesis of a family of atomic laminate metal borides with in-plane chemical ordering. *J. Am. Chem. Soc.* **142**, 18583–18591 (2020).
26. Wang, J. *et al.* Discovery of hexagonal ternary phase Ti_2InB_2 and its evolution to layered boride TiB . *Nat. Comm.* **10**, 2284 (2019).
27. Chakraborty, P., Chakrabarty, A., Dutta, A. & Saha-Dasgupta, T. Soft MAX phases with boron substitution: A computational prediction. *Phys. Rev. Mater.* **2**, 103605 (2018).
28. Zhou, J. *et al.* Boridene: Two-dimensional $Mo_{4/3}B_{2-x}$ with ordered metal vacancies obtained by chemical exfoliation. *Science* **373**, 801–805 (2021).
29. Zhang, D. *et al.* Experimental and theoretical investigation of the damage evolution of irradiated $MoAlB$ and $WAlB$ MAB phases. *J. Alloy. Compd.* **942**, 169099 (2023).
30. Kota, S. *et al.* Synthesis and characterization of the atomic laminate Mn_2AlB_2 . *J. Eur. Ceram. Soc.* **38**, 5333–5340 (2018).
31. Kota, S. *et al.* Magnetic properties of Cr_2AlB_2 , Cr_3AlB_4 , and CrB powders. *J. Alloy. Compd.* **767**, 474–482 (2018).
32. Ade, M. & Hillebrecht, H. Ternary borides Cr_2AlB_2 , Cr_3AlB_4 , and Cr_4AlB_6 : The first members of the series $(CrB_2)_nCrAl$ with $n = 1, 2, 3$ and a unifying concept for ternary borides as MAB-phases. *Inorg. chemistry* **54**, 6122–6135 (2015).
33. Carlsson, A., Rosen, J. & Dahlqvist, M. Theoretical predictions of phase stability for orthorhombic and hexagonal ternary MAB phases. *Phys. Chem. Chem. Phys.* **24**, 11249–11258 (2022).
34. Koutná, N., Hultman, L., Mayrhofer, P. H. & Sangiovanni, D. G. Phase stability and mechanical property trends for mab phases by high-throughput ab initio calculations. *Mater. & Des.* **241**, 112959 (2024).
35. Khazaei, M. *et al.* Novel MAB phases and insights into their exfoliation into 2D MBenes. *Nanoscale* **11**, 11305–11314 (2019).
36. Berastegui, P., Riekehr, L. & Jansson, U. Magnetron sputtering of nanolaminated Cr_2AlB_2 . *Coatings* **10**, 735 (2020).
37. Chen, Y., Kota, S., Barsoum, M. W. & Radovic, M. Compressive deformation of $MoAlB$ up to 1100°C. *J. Alloy. Compd.* **774**, 1216–1222 (2019).
38. Achenbach, J.-O. *et al.* Synthesis and properties of orthorhombic $MoAlB$ coatings. *Coatings* **9**, 510 (2019).
39. Evertz, S., Pöllmann, P., Holzapfel, D. M., Mayer, E. & Schneider, J. M. Low temperature synthesis of dense $MoAlB$ thin films. *J. Eur. Ceram. Soc.* **41**, 6302–6308 (2021).
40. Sahu, R., Bogdanovski, D., Achenbach, J.-O., Schneider, J. M. & Scheu, C. Defects in an orthorhombic $MoAlB$ MAB phase thin film grown at moderate synthesis temperature. *Nanoscale* **14**, 2578–2585 (2022).
41. Roy, C., Mondal, S., Banerjee, P. & Bhattacharyya, S. Low temperature atmospheric synthesis of $WAlB$ and Mn_2AlB_2 mab phases by modified molten salt shielded synthesis method. *Adv. Powder Technol.* **34**, 103983 (2023).
42. Liu, J. *et al.* Rapid synthesis and characterization of a nanolaminated Fe_2AlB_2 compound. *J. Alloy. Compd.* **766**, 488–497 (2018).
43. Liu, Y., Jiang, Z., Jiang, X. & Zhao, J. New refractory MAB phases and their 2d derivatives: insight

- into the effects of valence electron concentration and chemical composition. *RSC advances* **10**, 25836–25847 (2020).
44. Dai, F.-Z., Feng, Z. & Zhou, Y. First-principles investigation on the chemical bonding, elastic properties and ideal strengths of MoAlB and WAlB nanolaminated mab phases. *Comput. Mater. Sci.* **147**, 331–337 (2018).
 45. Lind, H., Dahlqvist, M. & Rosen, J. In-plane ordered quaternary phases (i-MAB): electronic structure and mechanical properties from first-principles calculations. *J. Physics: Condens. Matter* **33**, 255402 (2021).
 46. Bai, Y. *et al.* Density functional theory insights into ternary layered boride MoAlB. *Acta Materialia* **132**, 69–81 (2017).
 47. Bai, Y. *et al.* Phase stability and weak metallic bonding within ternary-layered borides CrAlB, Cr₂AlB₂, Cr₃AlB₄, and Cr₄AlB₆. *J. Am. Ceram. Soc.* **102**, 3715–3727 (2019).
 48. Li, N. *et al.* Rapid synthesis, electrical, and mechanical properties of polycrystalline Fe₂AlB₂ bulk from elemental powders. *J. Am. Ceram. Soc.* **100**, 4407–4411 (2017).
 49. Lu, X. *et al.* Crack healing behavior of a MAB phase: MoAlB. *J. Eur. Ceram. Soc.* **39**, 4023–4028 (2019).
 50. Lu, X., Li, S., Zhang, W., Yu, W. & Zhou, Y. Thermal shock behavior of a nanolaminated ternary boride: MoAlB. *Ceram. Int.* **45**, 9386–9389 (2019).
 51. Bai, Y. *et al.* High-temperature mechanical properties and thermal shock behavior of ternary-layered MAB phases Fe₂AlB₂. *Int. J. Refract. Met. Hard Mater.* **80**, 151–160 (2019).
 52. Barsoum, M. W. Rippllocations: a progress report. *Front. Mater.* **7**, 146 (2020).
 53. Plummer, G. *et al.* On the origin of kinking in layered crystalline solids. *Mater. Today* **43**, 45–52 (2021).
 54. Kresse, G. & Furthmüller, J. Efficient iterative schemes for ab initio total-energy calculations using a plane-wave basis set. *Phys. Rev. B* **54**, 11169 (1996).
 55. Kresse, G. & Joubert, D. From ultrasoft pseudopotentials to the projector augmented-wave method. *Phys. Rev. B* **59**, 1758–1775 (1999).
 56. Perdew, J. P. *et al.* Restoring the density-gradient expansion for exchange in solids and surfaces. *Phys. Rev. Lett.* **100**, 136406 (2008).
 57. Parrinello, M. & Rahman, A. Polymorphic transitions in single crystals: A new molecular dynamics method. *J. Appl. Phys.* **52**, 7182–7190 (1981).
 58. Sangiovanni, D. G., Tasnádi, F., Johnson, L. J. S., Odén, M. & Abrikosov, I. A. Strength, transformation toughening, and fracture dynamics of rocksalt-structure Ti_{1-x}Al_xN (0 ≤ x ≤ 0.75) alloys. *Phys. Rev. Mater.* **4**, 033605 (2020).
 59. Sangiovanni, D. G., Mellor, W., Harrington, T., Kaufmann, K. & Vecchio, K. Enhancing plasticity in high-entropy refractory ceramics via tailoring valence electron concentration. *Mater. Des.* **209**, 109932 (2021).
 60. Koutná, N. *et al.* Atomistic mechanisms underlying plasticity and crack growth in ceramics: a case study of AlN/TiN superlattices. *Acta Materialia* **229**, 117809 (2022).
 61. Shapeev, A. V. Moment tensor potentials: A class of systematically improvable interatomic potentials. *Multiscale Model. & Simul.* **14**, 1153–1173 (2016).
 62. Fletcher, R. *Practical methods of optimization* (John Wiley & Sons, 2013).
 63. Podryabinkin, E., Garifullin, K., Shapeev, A. & Novikov, I. MLIP-3: Active learning on atomic environments with moment tensor potentials. *J. Chem. Phys.* **159**, 084112 (2023).
 64. Thompson, A. P. *et al.* LAMMPS - a flexible simulation tool for particle-based materials modeling at the atomic, meso, and continuum scales. *Comp. Phys. Comm.* **271**, 108171 (2022).
 65. Mouhat, F. & Coudert, F.-X. Necessary and sufficient elastic stability conditions in various crystal systems. *Phys. Rev. B* **90**, 224104 (2014).
 66. Mukhamedov, B., Tasnadi, F. & Abrikosov, I. A. Machine learning interatomic potential for the low-modulus Ti-Nb-Zr alloys in the vicinity of dynamical instability. *arXiv preprint arXiv:2412.06270* (2024).
 67. Xie, S. R., Rupp, M. & Hennig, R. G. Ultra-fast interpretable machine-learning potentials. *npj Comput. Mater.* **9**, 162 (2023).
 68. Chen, Y. *et al.* Effects of three-dimensional Cu/Nb interfaces on strengthening and shear banding in nanoscale metallic multilayers. *Acta Materialia* **199**, 593–601 (2020).

69. Magnuson, M., Hultman, L. & Högberg, H. Review of transition-metal diboride thin films. *Vacuum* **196**, 110567 (2022).
70. Chen, Y. *et al.* Cross-interface growth mechanism of nanotwins in extremely high stacking-fault energy ceramic layer. *Acta Materialia* **257**, 119189 (2023).
71. Huang, Y. *et al.* Harvesting superior intrinsic plasticity in nitride ceramics with negative stacking fault energy. *Acta Materialia* 120774 (2025).
72. Tromas, C. *et al.* Nanoindentation-induced deformation twinning in MAX phase Ti_2AlN . *Acta Materialia* **227**, 117665 (2022).
73. Parent, S. *et al.* Atomic force microscopy and transmission electron microscopy identification of deformation twinning in the Cr_2AlC max phase. *Acta Materialia* **270**, 119836 (2024).
74. Gruber, J., Barsoum, M. W. & Tucker, G. J. Characterization of ripplocation mobility in graphite. *Mater. Res. Lett.* **8**, 82–87 (2020).